Research Article

Electrically Driven Reprogrammable Vanadium Dioxide Metasurface Using Binary Control for Broadband Beam Steering

Matthieu Proffit, Sara Pelivani, Pascal Landais, and A. Louise Bradley*

Cite This: https://doi.org/10.1021/acsami.2c10194

Read Online

| ACCESS | | Metrics & More | | Article Recommendations | | Supporting Information |

ABSTRACT: Resonant optical phased arrays are a promising way to reach fully reconfigurable metasurfaces in the optical and near-infrared (NIR) regimes with low energy consumption, low footprint, and high reliability. Continuously tunable resonant structures suffer from inherent drawbacks such as low phase range, amplitude-phase correlation, or extreme sensitivity that makes precise control at the individual element level very challenging. We computationally investigate 1-bit (binary) control as a mechanism to bypass these issues. We consider a metasurface for beam steering using a nanoresonator antenna and explore the theoretical capabilities of such phased arrays. A thermally realistic structure based on vanadium dioxide sandwiched in a metal–insulator–metal structure is proposed and optimized using inverse design to

enhance its performance at 1550 nm. Continuous beam steering over 90° range is successfully achieved using binary control, with excellent agreement with predictions based on the theoretical first-principles description of phased arrays. Furthermore, a broadband response from 1500 to 1700 nm is achieved. The robustness to the design manufacturing imperfections is also demonstrated. This simplified approach can be implemented to optimize tunable nanophotonic phased array metasurfaces based on other materials or phased shifting mechanisms for various functionalities.

KEYWORDS: vanadium dioxide, phased array, binary control, LIDAR, beam steering, inverse design, nanoresonator, reconfigurable metasurface
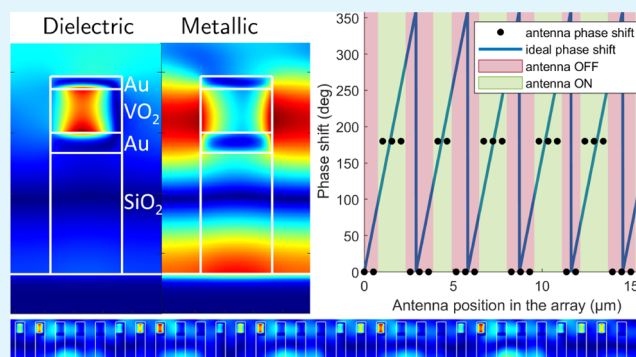
INTRODUCTION

Nanosized phased arrays are investigated for various near-infrared (NIR) or optical applications such as flat optics,[1] LIDAR,[2] or optical communications.[3] They require subwavelength control, which means nanoantennas capable of phase modulation must be engineered and manufactured. LIDAR systems still vastly rely on mechanical control that requires high precision and is slow and expensive. Photonics integrated circuits are being investigated[2,4,5] and offer promising improvements, but they still require individual calibration, high power consumption, and are complex structures to fabricate. The transfer of phased arrays from RF/mmW ranges to the optical domain[6] would enable a drastic reduction in cost, size, complexity, reliability, and energy consumption for LIDAR systems[2] and also enable a new generation of two-dimensional (2D) reconfigurable optical elements.[7]

One of the main ways to achieve this is by using the phase shift which occurs in a resonant antenna where light and matter strongly couple.[8−11] To tune the resonance, several parameters can be changed, many designs modify a geometric feature to achieve phase control with their response fixed at fabrication.[12,13] Some designs are switchable and possess two operating states[14−16] but to achieve a fully reconfigurable

device with a large number of degrees of freedom, each antenna must be individually controlled post-fabrication.[17] For a given geometry, one can change the material properties using the electro-optic effect,[8] carrier doping,[17−21] thermo-optic effect,[4] or phase-change materials like germanium–antimony–tellurium alloys (GST)[22−24] or vanadium dioxide (VO$_2$). GST-based resonant metasurfaces have been experimentally tested,[25] but the difficulties of experimentally changing its material have only recently been partially lifted.[26] VO$_2$ is one of the most promising materials to achieve phase change due to its significant change in optical properties and relative ease to trigger the material transition. Its insulator-to-metal transition (IMT) occurs around 68 °C over a range of temperatures,[27,28] wherein a mix of the two phases coexists to constitute an intermediate material. The structural phase change of vanadium dioxide from dielectric to metallic around
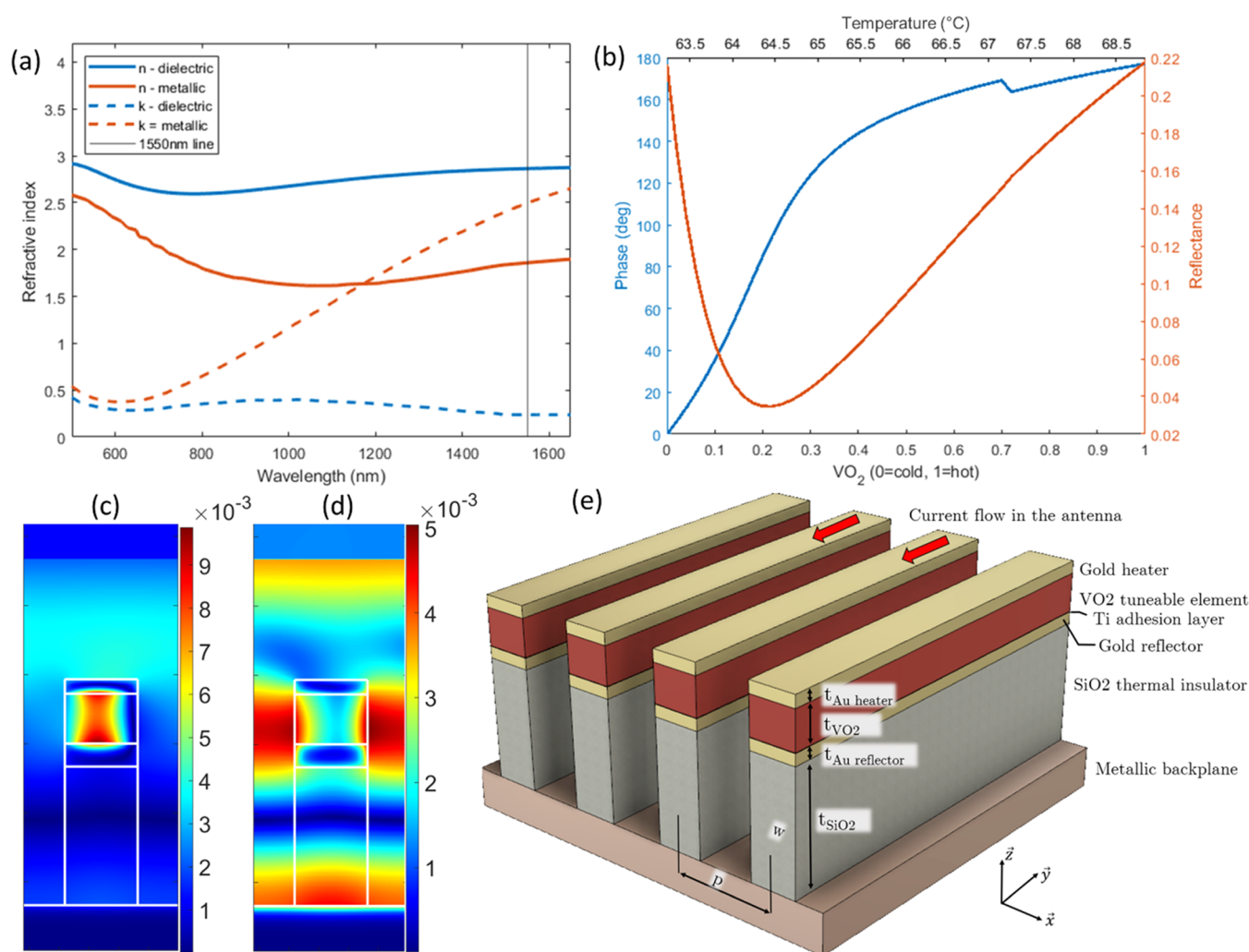
Figure 1. (a) Optical properties of VO_2 as a function of wavelength in cold (dielectric) and hot (metallic) states. These data were obtained using spectroscopic ellipsometry and are used for the FDTD simulations [see ref 32]. (b) Dependence of the output phase and reflectance at 1550 nm on the volume fraction of VO_2 in the hot state (which is proportional to the material temperature, see top x-axis) for a metasurface of identical antennas and an angle of incidence of 45°. (c, d) FDTD simulation at 1550 nm of the magnetic field H_y field in the antenna in its dielectric cold state and metallic hot state, respectively. (e) 3D structure schematic with design variables, materials, and coordinate system.

68 °C enables the development of tunable nanostructures for amplitude, polarization, or phase control. To date, several VO_2-based metasurface designs have been investigated by simulations[29] and experiments.[10,30] A continuous phase shift of up to 250 degrees at approximately 1550 nm has been achieved experimentally by thermally tuning a VO_2 nano-antenna array.[30] Many challenges remain in achieving this performance at the individual antenna scale. For example, one can mention mitigating thermal crosstalk between elements which prevents individual control or extending the phase shift range up to 2π. Furthermore, the resonant nature of the device poses two problems: the amplitude variations are not easily uncorrelated from the phase shift[17,29] and the phase shift varies very abruptly and nonlinearly[21] with temperature, which makes precise control of each element very challenging. It is possible to mitigate these limitations[31] at the cost of other performance indicators such as the maximum achievable phase shift or reflectance but they remain intrinsically linked to the resonant nature of the antennas.

Most of these difficulties arise from the fact that a continuous phase shift such as that implemented in radio-frequency phased arrays is targeted. However, what is feasible at the macroscale in the RF range may not be realistically applicable at the nanoscale. We propose to simplify the continuous phase shifting using 1-bit (binary) control of the array, the complexity, and most problems associated with resonant antennas are drastically reduced while control over the far-field amplitude pattern is retained.

In this paper, we introduce a metasurface based on a metal−insulator−metal (MIM) structure, which includes a layer of VO_2 as the tunable component. We use this example without loss of generality to consider a theoretical analysis of a binary controlled phased array metasurface, and we demonstrate that excellent properties for beam steering applications can be achieved. A continuum of anomalous reflection angles can be obtained over a wide angular range, and the beam shape and width do not differ from the continuous phase shift case. Binary control can be applied to metasurfaces composed of tunable antenna based on other materials and tuning mechanisms. We then optimize the individual MIM antenna for binary control in a VO_2 metasurface using inverse design, and emphasis is put on its thermal behavior both at the antenna and the array scale to ensure our design is tunable using Joule heating. This antenna is shown to have excellent

robustness regarding manufacturing inaccuracies and broadband response (1500−1700 nm) is achieved. We finally carry out finite difference time domain (FDTD) simulations to assess the performance of this nanoantenna design in an array and successfully demonstrate beam steering with excellent agreement with theory.

■ RESULTS AND DISCUSSION

Section I: Resonant Antenna Using VO₂. Vanadium dioxide is a material that exhibits a volatile structural change over a temperature range of around 68 °C.[32] A transition from a monoclinic arrangement to a tetragonal rutile structure occurs, which results in a drastic change in the complex refractive index as shown in Figure 1a,[33] especially in the infrared spectral range. This high material property modulation enables optical tuning with very little power consumption, unlike other phenomena such as the thermo-optic effect which is much smaller in magnitude and requires higher-temperature modulation to achieve a meaningful change in material properties. It has long been debated which phenomenon of the structural change (Peirls distortion) or the Mott insulator behavior is responsible for the large index change of VO₂ as they happen almost simultaneously.[34] The VO₂ transition can be triggered in many ways, including ultrafast optical excitation,[35] stress,[36] strain,[34] thermal excitation,[19,29] or electric current.[37] For beam steering, the simplest approach based on Joule heating is exploited. By applying a current in the gold heater (see Figure 1d), the temperature is locally raised to switch the VO₂ phase. Indirectly using current to trigger VO₂ transition avoids filamentation,[37] which occurs when a VO₂ element is directly subjected to a voltage. This percolative phenomenon is less reliable and presents limitations for implementation. The metasurface is composed of a MIM antenna with a period (p) of $\lambda/3$, a thermal insulation layer, and a conductive backplane. The layer thicknesses used throughout this paper are given in Table 1 and are the result of

Table 1. Antenna Design Parameters Values

variable	value (nm)
period, p	516.7 (fixed to $\lambda/3$)
width, w	245.2
t_{SiO_2}	600 (fixed)
t_{VO_2}	216.3
$t_{Au\ thermal}$	60 (fixed)
$t_{Au\ reflector}$	99.4
t_{Ti}	2 (fixed)

the thermal model and inverse design model which are detailed later in the paper. The phase and reflectance of the VO₂ metasurface, for 1550 nm x-polarized light incident at 45°, as a function of the volume fraction of metallic state VO₂ is shown in Figure 1b. As can be seen in Figure 1b, phase and amplitude cannot vary independently. This will result in additional side lobes in the far field, which has implications for phased array applications.[31] This antenna, optimized for a 180° phase shift, showcases a rather smooth phase shift with VO₂ composition and the minimum reflectance is not vanishingly small as observed when the total phase shift is maximized (when the resonance of the antenna coincides very precisely with the operating wavelength).

The resonance phenomenon in each of the antenna responsible for the phase shift can be seen in the field maps shown in Figure 1c,d. A magnetic dipole resonance is evident when the VO₂ layer is in the cold, dielectric state. The field map is slightly asymmetric due to the 45° angle of incidence. This resonance disappears when the VO₂ transitions to its metallic state. The antenna state closest to resonance is obtained for 20% of metallic VO₂ and has the lowest reflectance. The high intrinsic losses in VO₂ lead to this problem; however, the metasurface reflectance is higher when in a state further away from resonance. When the purely dielectric and purely metallic states have a reasonably high reflectance, the antenna are more suitable for binary control, as will be discussed further below. A similar design has previously been manufactured with a thinner SiO₂ layer; the fabrication protocol can be used for the structure studied herein.[4,38]

Section II: Binary Control. *Binary Control Principle.* Binary control has been proposed in the context of "programmable metasurfaces" or "coding metamaterials".[39] It has been investigated experimentally for a few applications ranging from holography[40] to 5G phased arrays.[41] Binary or 1-bit control consists in switching each antenna into one of two states using an external stimulus. In this case, the stimulus is Joule heating to trigger VO₂'s IMT and induce a phase shift in the scattered electromagnetic field. We only consider the states where VO₂ is purely in the cold monoclinic state or in the hot rutile state which simplifies thermal control drastically. $d\Phi/dT$ is easily above 90°/K, see Figure 1b, so instead of precisely tuning the individual temperature of each element to a high precision, we can have a cold point well below the IMT transition temperature (T_c) and a hot point above T_c. The volatile transition of VO₂ enables full reconfigurability of the array and dynamic beam steering at high frequencies.

The angular dependence of the electric field for a reflecting array in the Fraunhofer conditions is given by eq 1. It is a direct summation of each antenna's complex contribution at every angle in space. The geometry and parameters are shown in Figure 2a. We designate as θ_i and θ_r the angle of incidence and desired anomalous reflection, and Φ_m and $E_m(\theta)$ the phase delay and the amplitude pattern of the E-field emitted by the mth antenna (out of a total of N) located in the one-dimensional (1D) array at position $x = x_m$ at an angle θ, respectively.

$$E(\theta) = \sum_{m=1}^{N} E_m(\theta) e^{j(kx_m \sin(\theta_i) + kx_m \sin(\theta) + \Phi_m)} \tag{1}$$

For beam steering applications, the electric field from all antennas has to constructively interfere at a given angle as to maximize energy in that direction. The generalized law of refraction[1] given in eq 2 in a homogeneous medium gives the ideal phase shift profile for beam steering (derivation in the Supporting Information, Section I).

$$\sin(\theta_i) + \sin(\theta_r) = \frac{\lambda}{2\pi} \frac{d\Phi}{dx} \tag{2}$$

Integrating this equation gives a linear phase profile as in Figure 2b,d with a slope directly related to the anomalous reflection angle. It is directly applicable in ideal continuous phase shifting and requires 2π continuous phase shift capability. The binary control algorithm to convert this "ideal phase profile" is simple: we minimize the phase discrepancy between the binary phase shift profile and the ideal
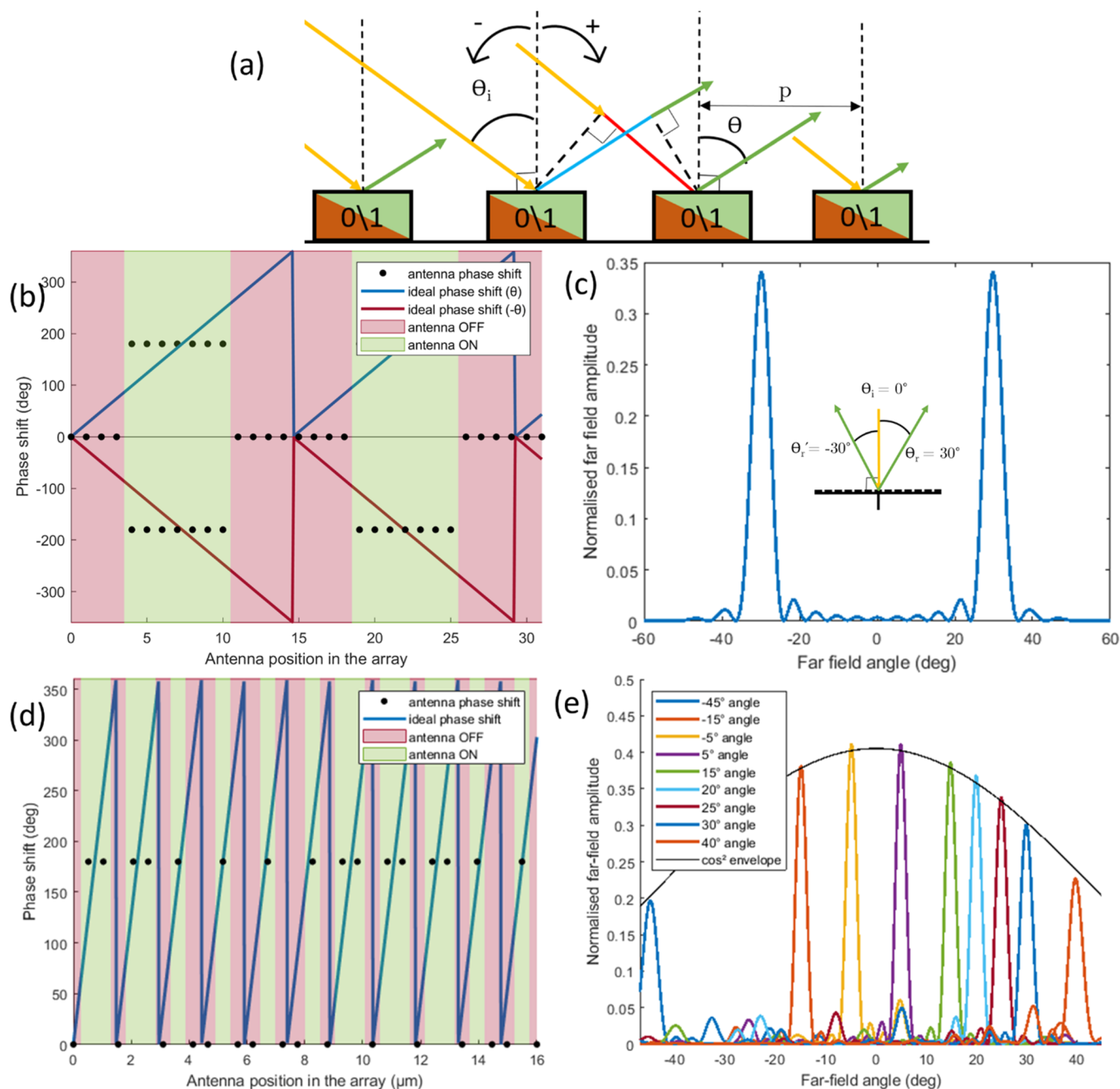
Figure 2. (a) Schematic of a sample binary phased array. (b) Illustration of the "−θ problem": the binary control algorithm calculates two different phase profiles and implements them mod(2π) for each antenna where each antenna is represented by a dot, it cannot distinguish between beam steering at θ_r and $-\theta_r$ as a phase shift of π and $-\pi$ corresponds to the same physical action. (c) Far-field pattern obtained with normal incident light and $\theta_r = 30°$. Inset: schematic of the array configuration. (d) Ideal phase profile and the corresponding antenna states with binary control for $\theta_i = 45°$ and $\theta_r = 20°$. This results in an aperiodic arrangement of ON and OFF antennas along the array. (e) Far-field pattern calculated for a fixed angle of incidence $\theta_i = 45°$, $N = 64$ antennas and using binary control to achieve various values of θ_r. The $\cos^2$ envelope corresponding to the antenna factor is shown to explain the lower amplitude at higher angles of anomalous reflection.

one. For $\Phi(x) \in [-\pi/2, \pi/2]$, we use a phase shift of 0 ("OFF" state, the VO$_2$ element is in its cold dielectric state) and, for $\Phi(x) \in [\pi/2, 3\pi/2]$, we have a π phase shift, the antenna is in "ON" state and the VO$_2$ element is in its hot metallic state. The phase shift is $\Phi(\text{Hot}) - \Phi(\text{Cold})$. This selection algorithm is simple and maximizes by construction the power at angle θ_r but simultaneously maximizes the power sent at $-\theta_r$ for normal incidence, $\theta_i = 0$. As can be seen in Figure 2b,c, binary control generates two symmetric beams, which would be a limitation for LIDAR applications. However,

it is technically possible to spatially filter out light in half of the hemisphere, but a better solution is to break this symmetry. These two beams correspond to $\sin(\theta_i) - \sin(\theta_r) = \pm\alpha$, where α is a continuously tunable parameter in $[-\lambda/2p; \lambda/2p]$ corresponding to the right-hand term of eq 2. Using non-normal incidence, we can displace this $-\theta_r$ beam out of a region of interest defined by $[-\theta_{\text{lim}}, \theta_{\text{lim}}]$. The optimal angle of incidence maximizing the angular range of this region depends on the array period relative to the wavelength and is given in eq 3 (derivation in the SI, Section II). Here, we use $p = \lambda/3$,
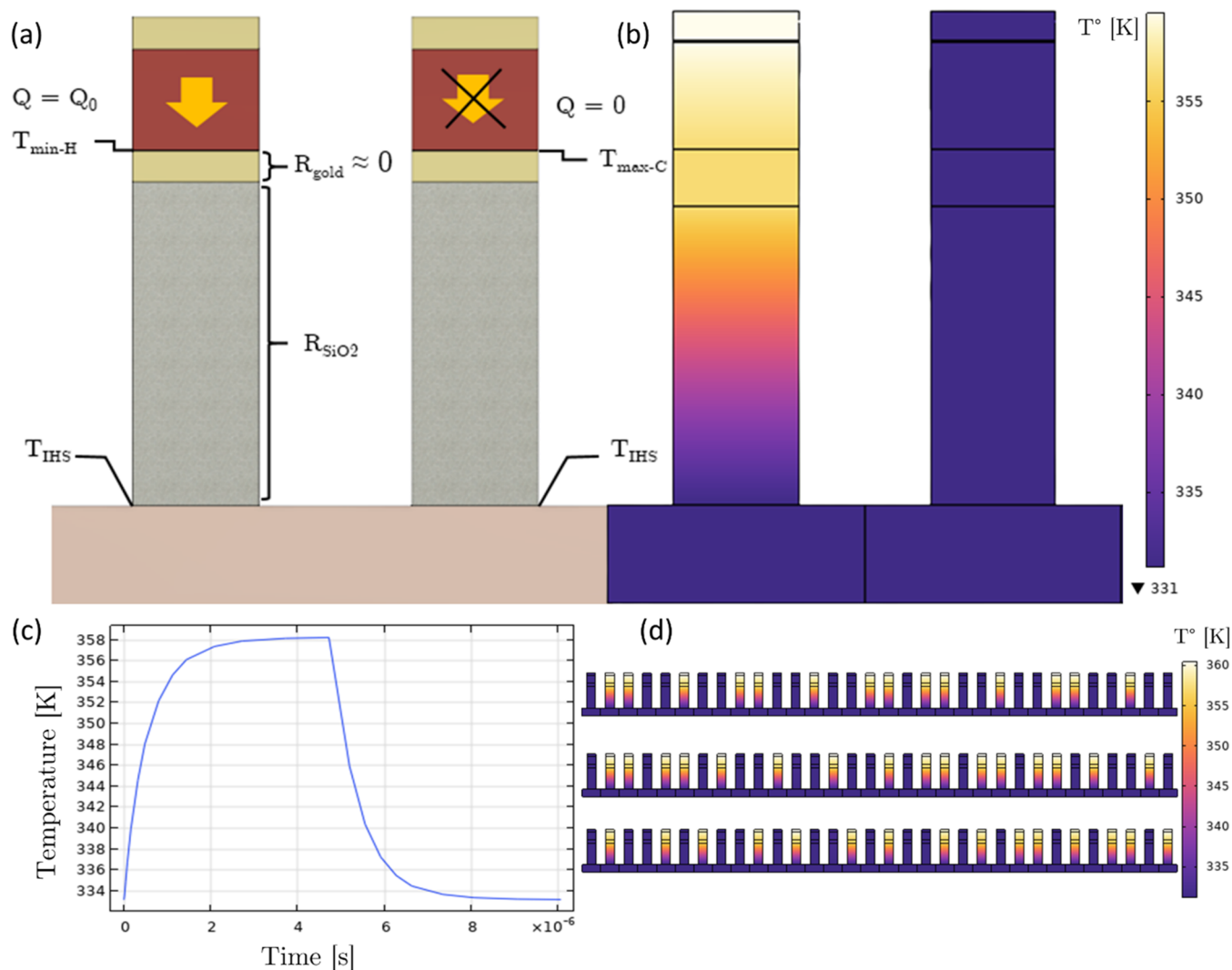
Figure 3. Thermal study. (a) Heat transfer diagram of the antenna-scale problem. (b) Finite element study of the antenna-scale problem, steady-state temperature distribution when only the left antenna is turned ON. (c) Transient behavior of the thermal contrast between two adjacent antennas in different states, 5 μs heat pulse applied. (d) Steady-state temperature distribution of three configurations with $N = 32$, $\theta_i = 45°$ (fixed), and varying values of θ_r, respectively, 10, 20, and 30° (top to bottom), we demonstrate excellent thermal contrast between adjacent antennas for all patterns.

which corresponds to $\theta_{lim} = 48.6°$. We round down to 45° to take the beam width into account and avoid a trailing edge of the $-\theta_r$ beam in the region of interest.

$$\theta_{lim} = -\theta_i = \arcsin\left(\frac{\lambda}{4p}\right) \tag{3}$$

As the phase gradient shown in Figure 2d can be continuously tuned by the ON−OFF pattern we can see in Figure 2e that it is possible to obtain any angle of anomalous refraction with binary control within $[-\theta_{lim}, \theta_{lim}]$. A given phase gradient usually results in an aperiodic antenna state arrangement, the number of possible arrangements specific to beam steering scales with N^2 (where N is the number of antennas), faster than the number of resolvable points and not logarithmically as for periodic arrangements. Even for low values of N, the number of possible array configurations greatly exceeds the number of resolvable points. Even if a discrete number of anomalous reflection angles is achieved, the beam steering is effectively continuous (see the SI, Section V). In the general case where the array is in a nonperiodic arrangement, the beam

intensity $I_{max} = I_{ideal} (2/\pi)^2$ (approximately 0.405 of the ideal case, derivation in the SI, Section IV), this reduction in amplitude in the far field is due to partially destructive interference induced by the discretization for binary control. Simulations show that for $\theta \approx \theta_r$, binary and continuous control have a similar beam shape within a multiplicative constant. The FWHM remains the same as for continuous control and is given in eq 4.[42] We can see that the FWHM depends on the span $(N \cdot p)$ of the array relative to the wavelength, decreasing the array period will be counterproductive in that regard. With the array period $p = \lambda/3$, at normal incidence $(\theta = 0)$ with $N = 32$, we have FWHM = 4.8 and 2.4° with $N = 64$.

$$\Delta_{FWHM} = \frac{0.886\lambda}{Np \cos(\theta)} \tag{4}$$

Section II: Antenna Design. *Thermal Design.* Deposited vanadium dioxide thin films are inhomogeneous structures that require a precise understanding of their microstructure to explain their optical behavior.[32] The film's microstructure

grain boundaries and defect densities are the two main factors that dictate the thermal hysteresis and transition width.[28] In addition, adhesion to the substrate induces strain in the first few nanometers of the film, which further complicates the thermal response. Hysteresis and transition width can be engineered up to a certain point. The MIM VO$_2$ array would benefit from a swift transition that requires the smallest thermal contrast between adjacent antennas, while ensuring one can be in the fully semiconducting VO$_2$ state while the other is in the fully metallic VO$_2$ state. We take a very conservative approach and design for a temperature contrast $\Delta T = T_{\text{min-H}} - T_{\text{max-C}} = 25$ °C. This number could be potentially reduced depending on the VO$_2$ layer properties and other manufacturing or engineering factors.

As described earlier, the beam steering metasurface under consideration is based on a MIM structure, with additional layers added for thermal purposes as shown in Figure 1d. Two thermal challenges have to be addressed at different scales. At the antenna scale, thermal crosstalk must be prevented; this is not a trivial task as it requires maintaining a temperature difference of 25° over a few hundreds of nanometers. At the array scale, the heat generated by all of the antennas must be dissipated. While the absolute power is relatively low (a few W), the heat flux is very high (~2000 W/cm^2, see the SI, Section VI).

The antenna-scale heat problem is summarized in Figure 3a in a heat transfer diagram; it is a 2D problem as the antenna cross section does not vary along its length. The detailed solution to this problem can be found in the SI (Section IV). The minimum thermal insulator thickness necessary to ensure a thermal contrast ΔT can be calculated using eq 5

$$t_{\text{insulator}} = \frac{\Delta T k}{t_{\text{Au}} Q_{\text{vol}}} \qquad (5)$$

where k is the thermal conductivity of the insulator and Q_{vol} is the volumetric heat generation in W/m^3. This value is set to 9.76×10^{14}, which corresponds to a current density of 2×10^{11} A/m^2, 10 times less than the experimental limit.[43] It is best to maximize Q_{vol} to reduce the insulator thickness, but we chose a high safety factor to ensure the feasibility of the thermal design. The failure mechanisms for nanowires are very different from bulk and are size-dependent; the value mentioned above may need to be adjusted for different designs if the wire dimension changes. The SiO$_2$ thickness can be reduced by increasing the heat generation; the value of $t_{\text{Au}} = 60$ nm was found to be a good compromise between optical properties (which favors lower Au thickness as we will see later) and thermal performance (more heat generation with higher heater thickness). SiO$_2$ is a very convenient material choice as it is easily deposited, and its low thermal conductivity of 1.4 W/mK thins down the insulating layer. With these parameters, a SiO$_2$ insulating layer of 600 nm is required to obtain $\Delta T = 25°$.

The steady-state temperature distribution in the array has been calculated using the commercially available finite element code COMSOL, as shown in Figure 3b. The internal heat spreader (IHS) temperature is set to $T_{\text{IHS}} = 58$ °C = $T_c - 10$ °C, the convective heat transfer with ambient air is negligible at the antenna scale. The thermal contrast in the simulations agrees well with the calculations, and the small discrepancy is due to the gold thickness whose thermal resistance and conduction in the substrate are neglected in our calculation. The transient behavior has similarly been modeled and is

presented in Figure 3c; we find a very fast settling time, of the order of 2−3 μs, which could be expected given the high energy density in the device. Thermal simulations conducted at the array scale are shown in Figure 3d with different binary control patterns; they correspond (top to bottom) to an anomalous reflection angle θ_r of 10, 20, and 30°, respectively, for a fixed angle of incidence $\theta_i = 45°$.

The array scale heat dissipation problem has already been studied intensively by microprocessor manufacturers,[44] and the use of internal heat spreaders IHS is generally employed in the industry to cool down small components like this array. The idea is to spread the heat in a conductive plate to dissipate it over a larger surface area. An efficient IHS is necessary to cool down the array without resorting to more complex cooling methods, such as the use of cryogenics, liquids, and enhanced forced convection, for example. This means a thermally conductive substrate is required; hence, the use of a gold backplane in this structure. SiO$_2$ or other insulating materials are not suitable. The results of IHS model calculations (detailed in the SI, Section IV) are shown in Table 2, and

Table 2. Temperature Increase: IHS Model Comparison to Finite Element Simulation for an Array-Scale Cooling Problem

method	ΔT_{avg}	ΔT_{max}
IHS model	31.87	32.06
finite element	31.54	31.77

compared to the finite element results. They validate the fact the array can be cooled down efficiently without resorting to advanced methods. ΔT_{avg} corresponds to the average temperature increase in the array, and ΔT_{max} corresponds to the maximum temperature increase (usually at the center of the array where heat dissipation is the most difficult to achieve). For a fixed set of cooling conditions, there will be an array size where the operating point will be above the VO$_2$ transition temperature, rendering it ineffective. As can be seen in SI Section IV, the heat generated scales linearly with the antenna length but so does the heat dissipated through the backplane (as an IHS). The length of the antenna does not impact the temperature increase in a heated antenna. However, it does impact the total amount of heat generated by the array. In the SI, we considered a square array where the length of the antenna is equal to the array width ($=N \cdot p$) and we observe an increase in the array temperature with increasing N. The energy consumption of an individual antenna is calculated in the SI. In SI Section IX, we briefly discuss the wiring of the individual antenna and the impact on energy consumption and heat generation. It is shown that heat generation in the contact wires can be neglected in the IHS calculations.

Inverse Design. Now that we have set several design parameters to obtain a functional binary controlled phased array, we can optimize the structure to maximize its performance while respecting the aforementioned engineering constraints. To conduct this multiparameter optimization, we employ inverse design. Machine learning has opened new possibilities in many fields, and its applications in photonics are just starting to be explored.[26,45] Inverse design lets an algorithm adjust some degrees of freedom (DOF) to optimize a user-designed figure of merit (FOM). This allows for multiple DOF simultaneous optimization. There are many algorithms that can be used to optimize a structure. Given the
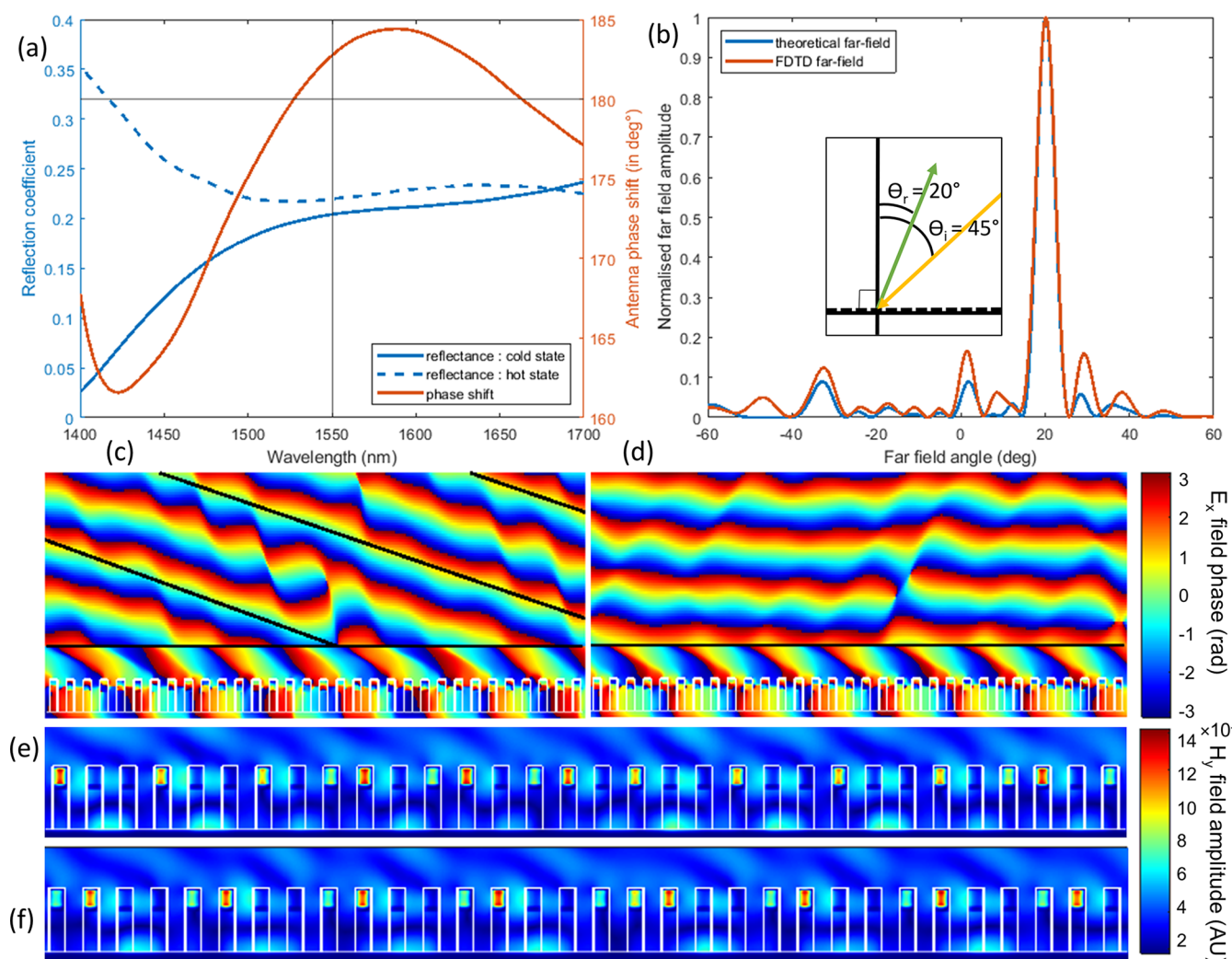
Figure 4. Array-scale FDTD simulation results. (a) Broadband properties of the antenna, the reflectance in each state, and the phase shift added between the hot and cold states, $\Phi(\text{Hot}) - \Phi(\text{Cold})$, are shown between 1400 and 1700 nm, the slight difference at 1550 nm with Figure 1b arises from the interpolation of the material dispersion in Lumerical, whereas a single wavelength was used for the simulation at 1550 nm in Figure 1b. (b) Normalized far-field amplitude as a function of angle calculated using FDTD simulations (red) compared to the direct theoretical E-field distribution from eq 1, for incident angle $\theta_i = 45°$, and desired reflection angle $\theta_r = 20°$. Inset: schematic showing the angles of incidence and reflection on the array. (c, d) Ex field phase for $\theta_i = 45°$, $\theta_r = 20$ and $0°$, respectively; we can clearly see beam steering even in the near field. The horizontal black line materializes the source position; we see the incident wave below the source and the reflected field above. (e, f) H_y field amplitude for $\theta_i = 45°$, $\theta_r = 20°$ (e) and $0°$ (f), respectively; we can compare this figure to Figure 2d and easily see the antennas in the cold state exhibit a magnetic dipole resonance in the VO$_2$ element.

specifics of this case, the hybrid PSO—interior-point algorithm is the most relevant (more details can be found in the SI, Section VIII). The gold heater thickness is fixed as the inverse design algorithm finds better performance with lower thickness values that are incompatible with our thermal constraints. A value $t_{\text{Au thermal}} = 60$ nm is a good compromise between energy consumption, thermal contrast, and reflectance efficiency. The only values that are optimized here are therefore the antenna width w, the VO$_2$ thickness t_{VO_2}, and the gold reflector thickness $t_{\text{Au reflector}}$.

Binary control is ideally implemented with a maximized phase contrast of π while maintaining the amplitude ratio of 1 between the two antenna states. The FOM given in eq 6 is calculated for a given antenna structure from two simulations carried out with the VO$_2$ in dielectric and rutile states. The FOM is the product of two terms that have to be maximized simultaneously.

$$\text{FOM} = \text{gauss}(\pi, \pi/9) \cdot \min(R_{\text{ON}}, R_{\text{OFF}}) \qquad (6)$$

The first term is a Gaussian centered at $180°$ with a standard deviation of $20°$ (arbitrary value) to maximize the phase contrast between both states with vanishing values when the phase shift is far from π. The second term is the minimum reflectance of both states; this incentivizes the algorithm to increase only the state with minimum reflectance to reduce the amplitude discrepancy. Eventually, this FOM component also increases the overall reflectance, but unlike any other formula (geometric mean or arithmetic mean, for example), it does not push the algorithm to increase the reflectance of one state at the expense of the other. Note that it is better for our array performance to have a 0-reflectance discrepancy rather than a higher reflectance in a single state to avoid side lobes. The hybrid inverse design algorithm results can be found in Table 1; these are optimal values as defined by our FOM and within the engineering bounds we have specified. As it is a versatile

G

algorithm, we also show results in the SI for alternative geometries that could correspond to other engineering choices and their associated performances. The optimization algorithm can be applied to finding structures suitable for different criteria such as operating wavelength, material properties, and even applications. Examples of geometries optimized for different parameters are shown in the SI (Section VIII).

Section III: Antenna Performance. The geometry prescribed in Table 1 has been assessed thoroughly using the commercially available finite difference time domain software Lumerical. As reported by other studies, this resonance causes a phase shift in the reflected beam and also decreases the reflectance to 21% due to the strong light−matter interaction in dissipative materials, as seen in Figure 1b. The broadband performance of the array is assessed and presented in Figure 4a. The metasurface, despite the resonant behavior of each antenna maintains its performance over a wide band, especially above its operating wavelength of 1550 nm for up to 100 nm. This broadband performance allows the structure to remain functional for binary control including when we account for manufacturing inaccuracies that can modify the resonant wavelength of the system (see SI, Section VII).

Now that the antenna geometry is optimized, the metasurface is programmed using binary control with some antennas turned ON and some others turned OFF. The results for the FDTD simulation of a full array with $N = 32$ elements, an angle of incidence $\theta_i = 45°$, and the desired reflection angle $\theta_r = 20°$ are presented in Figure 4b. The overall reflectance of the metasurface is ∼8%, determined by the reflectance of the antenna (21%) times the peak power ratio for binary control (∼0.4), as described in SI Section IV. Beam steering performance can also be quantified by the optical directivity, defined as the ratio of the intensity at the desired angle θ_r to the power radiated in all directions normalized by the solid angle.[46] The optical directivity calculated for $N = 32$ with binary control is 19.6 versus 31.3 for the ideal case. These values increase to 41.4 and 62.8, respectively, with $N = 64$. The far-field pattern obtained from the simulations is also compared to first-principles calculations using eq 1. Figure 4c,d shows the beam steering patterns, and more specifically, Figure 4e,f shows the magnetic dipole resonance in each antenna in the cold state. Excellent agreement of the theoretical model with numerical simulations is obtained demonstrating that electromagnetic crosstalk remains limited, and the antenna's performance is unchanged when placed in an array with adjacent antennas in a different state. Given the broadband response of the metasurface, a scheme employing wavelength multiplexing to scan several angles at once could be considered. The antenna behaves close to a perfect binary antenna with π phase shift and near-unity amplitude ratio of the reflectance in the cold and hot states over a broad wavelength band. If the incident beam contains multiple wavelengths, the anomalous reflection will separate them, which could be used to increase the scanning speed, for example, in LiDAR applications. This could enable another degree of freedom to steer the beam around a second axis by tuning the illumination wavelength.[47]

Binary control can be applied without any loss of generality to any phased array regardless of the mechanism used to tune the output phase. For example, this approach can be applied to phased arrays using other PCMs or external phase shifters at any wavelength and scale. All of the analytical derivations have been presented in 1D but can easily be extended to 2D

metasurfaces (see SI Section III), though it is noted that the antenna design considered herein cannot be easily implemented in an electrically driven 2D metasurface. Furthermore, one can note that we have only considered a structurally periodic (with uniform antenna spacing) phased array with uniform illumination (all of the antennas are subjected to the same incident field amplitude); this kind of device is not known for its optimal performance. Structurally aperiodic arrays tend to perform better in practice,[48] and amplitude tapering is also very useful to reduce side lobes intensity. We did not extend the analysis to these special phased arrays to keep the analysis as reproducible and general as possible, but performance in applications can be further improved using these concepts. While structural aperiodicity may prove to be more taxing to achieve, as changing the gap between adjacent antennas may influence their response, amplitude tapering is almost guaranteed as the illumination from a laser source has a nonconstant beam amplitude profile by nature. Array-level inverse design[46] could also be implemented to improve the binary control algorithm with a possibility to enhance user-defined properties of the far field. Finally, the simple inverse design algorithm exploited to tune the antenna parameters could be used with another set of engineering constraints or FOM to get a different functionality.

■ CONCLUSIONS

We have successfully applied binary control to phase-change nanoantenna arrays. It is seen that this approach provides a solution to many of the issues that have been encountered in the practical implementation of tunable resonant phased array metasurfaces in the NIR and optical domains. The performance decrease compared to ideal continuous control is compensated by an easy implementation based on a control of the binary state of each antenna. This approach can be applied to tunable metasurfaces for a wide range of applications. A thermally realistic VO_2-based MIM antenna has been investigated. Using binary control, combined, with inverse design at the antenna level within feasible engineering limits, broadband continuous beam steering over a 90° angular range between 1500 and 1700 nm has been demonstrated. It is expected that inverse design and machine learning at the antenna and array levels will reveal designs capable of high performance coupled with less demanding implementation requirements for a wide range of metasurface wavefront engineering challenges and applications.

■ METHODS

The behavior of the proposed structure was studied using the Ansys Lumerical software for FDTD simulations. Given the symmetry of the antenna structure, we studied a 2D cross section. Several mesh refinements were created to fit the mesh boundaries with the material boundaries; the x and y mesh sizes are 10 and 12 nm, respectively (this was adjusted to have an exact integer number of mesh cells in each material layer). No significant variation in the results was found with a smaller mesh size. This procedure avoids the staircase effect and enables small variations in the design to be measured in the FOM, which is of prime importance for the implementation of the inverse design algorithm. Because of the non-normal incidence angle, Bloch boundary conditions (BC) were used on the x-axis instead of periodic BC. Perfectly matched layers (PML) were used on the y-BC to emulate an optically thick backplane on the z-min boundary and a semi-infinite free space on the z-max boundary. All of the simulations except the broadband characterization (in Figure 4a) were narrowband to reduce the interpolation errors on the material

dispersion curves. The material properties of intermediate VO$_2$ phases for Figure 1b were calculated using the Bruggeman effective medium approximation.[30]

■ ASSOCIATED CONTENT

ⓢ Supporting Information

The Supporting Information is available free of charge at https://pubs.acs.org/doi/10.1021/acsami.2c10194.

Derivation and proof of equations, detailed heat transfer calculations, and more simulation results (PDF)

■ AUTHOR INFORMATION

Corresponding Author

A. Louise Bradley − *School of Physics and AMBER, Trinity College Dublin, Dublin 2, Ireland; IPIC, Tyndall National Institute, Cork T12R5CP, Ireland;* ⓞ orcid.org/0000-0002-9399-8628; Email: bradlel@tcd.ie

Authors

Matthieu Proffit − *School of Physics and AMBER, Trinity College Dublin, Dublin 2, Ireland;* ⓞ orcid.org/0000-0002-1846-4474

Sara Pelivani − *School of Physics and AMBER, Trinity College Dublin, Dublin 2, Ireland*

Pascal Landais − *School of Electronic Engineering, Dublin City University, Dublin 9, Ireland*

Complete contact information is available at:
https://pubs.acs.org/10.1021/acsami.2c10194

Author Contributions

The manuscript was written through contributions of all authors. All authors have given approval to the final version of the manuscript.

Funding

Notes

The authors declare no competing financial interest.

■ ACKNOWLEDGMENTS

■ REFERENCES

(1) Yu, N.; Genevet, P.; Kats, M. A.; Aieta, F.; Tetienne, J.-P.; Capasso, F.; Gaburro, Z. Light Propagation with Phase Discontinuities: Generalized Laws of Reflection and Refraction. *Science* **2011**, *334*, 333−337.

(2) Hsu, C.-P.; Li, B.; Solano-Rivas, B.; Gohil, A. R.; Chan, P. H.; Moore, A. D.; Donzella, V. A Review and Perspective on Optical Phased Array for Automotive LiDAR. *IEEE J. Sel. Top. Quantum Electron.* **2021**, *27*, 1−16.

(3) He, J.; Dong, T.; Xu, Y. Review of Photonic Integrated Optical Phased Arrays for Space Optical Communication. *IEEE Access* **2020**, *8*, 188284−188298.

(4) Chul Shin, M.; Mohanty, A.; Watson, K.; Bhatt, G. R.; Phare, C. T.; Miller, S. A.; Zadka, M.; Lee, B. S.; Ji, X.; Datta, I.; Lipson, M. Chip-Scale Blue Light Phased Array. *Opt. Lett.* **2020**, *45*, 1934−1937.

(5) Kim, T.; Bhargava, P.; Poulton, C. V.; Notaros, J.; Yaacobi, A.; Timurdogan, E.; Baiocco, C.; Fahrenkopf, N.; Kruger, S.; Ngai, T.; Timalsina, Y.; Watts, M. R.; Stojanović, V. A Single-Chip Optical Phased Array in a Wafer-Scale Silicon Photonics/CMOS 3D-Integration Platform. *IEEE J. Solid-State Circuits* **2019**, *54*, 3061−3074.

(6) Heck, M. J. R. Highly Integrated Optical Phased Arrays: Photonic Integrated Circuits for Optical Beam Shaping and Beam Steering. *Nanophotonics* **2017**, *6*, 93−107.

(7) Kamali, S. M.; Arbabi, E.; Arbabi, A.; Faraon, A. A Review of Dielectric Optical Metasurfaces for Wavefront Control. *Nanophotonics* **2018**, *7*, 1041−1068.

(8) Klopfer, E.; Dagli, S.; Barton, D.; Lawrence, M.; Dionne, J. A. High-Quality-Factor Silicon-on-Lithium Niobate Metasurfaces for Electro-Optically Reconfigurable Wavefront Shaping. *Nano Lett.* **2022**, *22*, 1703−1709.

(9) Chen, H.-T.; Padilla, W. J.; Cich, M. J.; Azad, A. K.; Averitt, R. D.; Taylor, A. J. A Metamaterial Solid-State Terahertz Phase Modulator. *Nat. Photonics* **2009**, *3*, 148−151.

(10) Hashemi, M. R. M.; Yang, S.-H.; Wang, T.; Sepúlveda, N.; Jarrahi, M. Electronically-Controlled Beam-Steering through Vanadium Dioxide Metasurfaces. *Sci. Rep.* **2016**, *6*, No. 35439.

(11) Ding, F.; Pors, A.; Bozhevolnyi, S. I. Gradient Metasurfaces: A Review of Fundamentals and Applications. *Rep. Prog. Phys.* **2017**, *81*, No. 026401.

(12) Zou, L.; Withayachumnankul, W.; Shah, C. M.; Mitchell, A.; Bhaskaran, M.; Sriram, S.; Fumeaux, C. Dielectric Resonator Nanoantennas at Visible Frequencies. *Opt. Express* **2013**, *21*, 1344−1352.

(13) Segal, N.; Keren-Zur, S.; Hendler, N.; Ellenbogen, T. Controlling Light with Metamaterial-Based Nonlinear Photonic Crystals. *Nat. Photonics* **2015**, *9*, 180−184.

(14) de Galarreta, C. R.; Alexeev, A.; Bertolotti, J.; Wright, C. D.*Phase-Change Metasurfaces for Dyamic Beam Steering and Beam Shaping in the Infrared*, 2018 IEEE International Symposium on Circuits and Systems (ISCAS), 2018; pp 1−5.

(15) de Galarreta, C. R.; Alexeev, A. M.; Au, Y.-Y.; Lopez-Garcia, M.; Klemm, M.; Cryan, M.; Bertolotti, J.; Wright, C. D. Nonvolatile Reconfigurable Phase-Change Metadevices for Beam Steering in the Near Infrared. *Adv. Funct. Mater.* **2018**, *28*, No. 1704993.

(16) Li, X.; Tang, S.; Ding, F.; Zhong, S.; Yang, Y.; Jiang, T.; Zhou, J. Switchable Multifunctional Terahertz Metasurfaces Employing Vanadium Dioxide. *Sci. Rep.* **2019**, *9*, No. 5454.

(17) Shirmanesh, G. K.; Sokhoyan, R.; Wu, P. C.; Atwater, H. A. Electro-Optically Tunable Multifunctional Metasurfaces. *ACS Nano* **2020**, *14*, 6912−6920.

(18) Huang, Y.-W.; Lee, H. W. H.; Sokhoyan, R.; Pala, R. A.; Thyagarajan, K.; Han, S.; Tsai, D. P.; Atwater, H. A. Gate-Tunable Conducting Oxide Metasurfaces. *Nano Lett.* **2016**, *16*, 5319−5325.

(19) Park, J.; Kang, J.-H.; Kim, S. J.; Liu, X.; Brongersma, M. L. Dynamic Reflection Phase and Polarization Control in Metasurfaces. *Nano Lett.* **2017**, *17*, 407−413.

(20) Iyer, P. P.; Butakov, N. A.; Schuller, J. A. Reconfigurable Semiconductor Phased-Array Metasurfaces. *ACS Photonics* **2015**, *2*, 1077−1084.

(21) Forouzmand, A.; Mosallaei, H. Electro-Optical Amplitude and Phase Modulators Based on Tunable Guided-Mode Resonance Effect. *ACS Photonics* **2019**, *6*, 2860−2869.

(22) Cao, T.; Zheng, G.; Wang, S.; Wei, C. Ultrafast Beam Steering Using Gradient Au- Ge$_2$Sb$_2$Te$_5$ -Au Plasmonic Resonators. *Opt. Express* **2015**, *23*, 18029−18039.

(23) Chu, C. H.; Tseng, M. L.; Chen, J.; Wu, P. C.; Chen, Y.-H.; Wang, H.-C.; Chen, T.-Y.; Hsieh, W. T.; Wu, H. J.; Sun, G.; Tsai, D. P. Active Dielectric Metasurface Based on Phase-Change Medium. *Laser Photonics Rev.* **2016**, *10*, 986−994.

(24) Forouzmand, A.; Mosallaei, H. Dynamic Beam Control via Mie-Resonance Based Phase-Change Metasurface: A Theoretical Investigation. *Opt. Express* **2018**, *26*, 17948−17963.

(25) Chen, Y.; Li, X.; Sonnefraud, Y.; Fernández-Domínguez, A. I.; Luo, X.; Hong, M.; Maier, S. A. Engineering the Phase Front of Light with Phase-Change Material Based Planar Lenses. *Sci. Rep.* **2015**, *5*, No. 8660.

(26) Abdollahramezani, S.; Hemmatyar, O.; Taghinejad, M.; Taghinejad, H.; Krasnok, A.; Eftekhar, A. A.; Teichrib, C.; Deshmukh, S.; El-Sayed, M. A.; Pop, E.; Wuttig, M.; Alù, A.; Cai,

W.; Adibi, A. Electrically Driven Reprogrammable Phase-Change Metasurface Reaching 80% Efficiency. *Nat. Commun.* **2022**, *13*, No. 1696.

(27) Kaplan, G.; Aydin, K.; Scheuer, J. Dynamically Controlled Plasmonic Nano-Antenna Phased Array Utilizing Vanadium Dioxide [Invited]. *Opt. Mater. Express* **2015**, *5*, 2513−2524.

(28) Suh, J. Y.; Lopez, R.; Feldman, L. C.; Haglund, R. F. Semiconductor to Metal Phase Transition in the Nucleation and Growth of VO2 Nanoparticles and Thin Films. *J. Appl. Phys.* **2004**, *96*, 1209−1213.

(29) Kim, M.; Jeong, J.; Poon, J. K. S.; Eleftheriades, G. V. Vanadium-Dioxide-Assisted Digital Optical Metasurfaces for Dynamic Wavefront Engineering. *J. Opt. Soc. Am. B* **2016**, *33*, 980−988.

(30) Kim, Y.; Wu, P. C.; Sokhoyan, R.; Mauser, K.; Glaudell, R.; Kafaie Shirmanesh, G.; Atwater, H. A. Phase Modulation with Electrically Tunable Vanadium Dioxide Phase-Change Metasurfaces. *Nano Lett.* **2019**, *19*, 3961−3968.

(31) Cala' Lesina, A.; Goodwill, D.; Bernier, E.; Ramunno, L.; Berini, P. On the Performance of Optical Phased Array Technology for Beam Steering: Effect of Pixel Limitations. *Opt. Express* **2020**, *28*, 31637−31657.

(32) Qazilbash, M. M.; Tripathi, A.; Schafgans, A. A.; Kim, B.-J.; Kim, H.-T.; Cai, Z.; Holt, M. V.; Maser, J. M.; Keilmann, F.; Shpyrko, O. G.; Basov, D. N. Nanoscale Imaging of the Electronic and Structural Transitions in Vanadium Dioxide. *Phys. Rev. B* **2011**, *83*, No. 165108.

(33) Cunningham, S.; Hrelescu, C.; Bradley, A. L. Plasmonic Nanodiscs on Vanadium Dioxide Thin Films for Tunable Luminescence Enhancement. *Opt. Express* **2021**, *29*, 22288−22298.

(34) Shao, Z.; Cao, X.; Luo, H.; Jin, P. Recent Progress in the Phase-Transition Mechanism and Modulation of Vanadium Dioxide Materials. *NPG Asia Mater.* **2018**, *10*, 581−605.

(35) Cavalleri, A.; Tóth, Cs.; Siders, C. W.; Squier, J. A.; Ráksi, F.; Forget, P.; Kieffer, J. C. Femtosecond Structural Dynamics in ${\mathrm{VO}}_{2}$ during an Ultrafast Solid-Solid Phase Transition. *Phys. Rev. Lett.* **2001**, *87*, No. 237401.

(36) Tselev, A.; Luk'yanchuk, I. A.; Ivanov, I. N.; Budai, J. D.; Tischler, J. Z.; Strelcov, E.; Kolmakov, A.; Kalinin, S. V. Symmetry Relationship and Strain-Induced Transitions between Insulating M1 and M2 and Metallic R Phases of Vanadium Dioxide. *Nano Lett.* **2010**, *10*, 4409−4416.

(37) Berglund, C. N. Thermal Filaments in Vanadium Dioxide. *IEEE Trans. Electron Devices* **1969**, *16*, 432−437.

(38) Kim, Y. Light Modulation with Vanadium Dioxide-Based Optical Devices. Ph.D Thesis, California Institute of Technology, 2022.

(39) Cui, T. J.; Qi, M. Q.; Wan, X.; Zhao, J.; Cheng, Q. Coding Metamaterials, Digital Metamaterials and Programmable Metamaterials. *Light Sci. Appl.* **2014**, *3*, e218.

(40) Li, L.; Jun Cui, T.; Ji, W.; Liu, S.; Ding, J.; Wan, X.; Bo Li, Y.; Jiang, M.; Qiu, C.-W.; Zhang, S. Electromagnetic Reprogrammable Coding-Metasurface Holograms. *Nat. Commun.* **2017**, *8*, No. 197.

(41) Basavarajappa, V.; Exposito, B. B.; Cabria, L.; Basterrechea, J. Binary Phase-Controlled Multi-Beam-Switching Antenna Array for Reconfigurable 5G Applications. *EURASIP J. Wirel. Commun. Networking* **2019**, *2019*, 180.

(42) Acoleyen, K.; Bogaerts, W.; Jágerská, J.; Thomas, N.; Houdré, R.; Baets, R. Off-Chip Beam Steering with a One-Dimensional Optical Phased Array. *Opt. Lett.* **2009**, *34*, 1477−1479.

(43) Durkan, C.; Schneider, M. A.; Welland, M. E. Analysis of Failure Mechanisms in Electrically Stressed Au Nanowires. *J. Appl. Phys.* **1999**, *86*, 1280−1286.

(44) Lasance, C. J. M. How to Estimate Heat Spreading Effects in Practice. *J. Electron. Packag.* **2010**, *132*, No. 031004.

(45) Campbell, S. D.; Sell, D.; Jenkins, R. P.; Whiting, E. B.; Fan, J. A.; Werner, D. H. Review of Numerical Optimization Techniques for Meta-Device Design. *Opt. Mater. Express* **2019**, *9*, 1842−1863.

(46) Thureja, P.; Shirmanesh, G. K.; Fountaine, K. T.; Sokhoyan, R.; Grajower, M.; Atwater, H. A. Array-Level Inverse Design of Beam Steering Active Metasurfaces. *ACS Nano* **2020**, *14*, 15042−15055.

(47) Hutchison, D. N.; Sun, J.; Doylend, J. K.; Kumar, R.; Heck, J.; Kim, W.; Phare, C. T.; Feshali, A.; Rong, H. High-Resolution Aliasing-Free Optical Beam Steering. *Optica* **2016**, *3*, 887−890.

(48) Baggett, B. M. W. Optimization of Aperiodically Spaced Phased Arrays for Wideband Applications. MS Thesis, Virginia Polytechnic Institute and State University, 2011.